NGTS-21b: an inflated Super-Jupiter orbiting a metal-poor K dwarf

Douglas R. Alves, James S. Jenkins, Jose I. Vines, Louise D. Nielsen, Samuel Gill, Jack S. Acton, D. R. Anderson, Daniel Bayliss, François Bouchy, Hannes Breytenbach, et al.

Monthly Notices of the ROYAL ASTRONOMICAL SOCIETY

MNRAS **517,** 4447–4457 (2022) https://doi.org/10.1093/mnras/stac2884
Advance Access publication 2022 October 7

NGTS-21b: an inflated Super-Jupiter orbiting a metal-poor K dwarf

Douglas R. Alves [1,2★] James S. Jenkins,[2,3★] Jose I. Vines,[1] Louise D. Nielsen,[4] Samuel Gill,[5,6] Jack S. Acton,[7] D. R. Anderson [5,6] Daniel Bayliss [5,6] François Bouchy,[8] Hannes Breytenbach,[9,10] Edward M. Bryant [11] Matthew R. Burleigh,[7] Sarah L. Casewell,[7] Philipp Eigmüller,[12] Edward Gillen [13,14] Michael R. Goad,[7] Maximilian N. Günther,[15] Beth A. Henderson,[7] Alicia Kendall,[7] Monika Lendl [8] Maximiliano Moyano,[16] Ramotholo R. Sefako,[10] Alexis M. S. Smith,[12] Jean C. Costes,[17] Rosanne H. Tilbrook,[7] Jessymol K. Thomas,[10] Stéphane Udry,[8] Christopher A. Watson,[18] Richard G. West [5,6] Peter J. Wheatley [5,6] Hannah L. Worters[10] and Ares Osborn [5,6]

Affiliations are listed at the end of the paper

Accepted 2022 October 1. Received 2022 September 30; in original form 2022 August 16

ABSTRACT

We report the discovery of NGTS-21b , a massive hot Jupiter orbiting a low-mass star as part of the Next Generation Transit Survey (NGTS). The planet has a mass and radius of $2.36 \pm 0.21\,M_{\rm J}$ and $1.33 \pm 0.03\,R_{\rm J}$, and an orbital period of 1.543 d. The host is a K3V ($T_{\rm eff} = 4660 \pm 41$ K) metal-poor ([Fe/H] $= -0.26 \pm 0.07$ dex) dwarf star with a mass and radius of $0.72 \pm 0.04\,{\rm M}_{\odot}$ and $0.86 \pm 0.04 R_{\odot}$. Its age and rotation period of $10.02^{+3.29}_{-7.30}$ Gyr and 17.88 ± 0.08 d, respectively, are in accordance with the observed moderately low-stellar activity level. When comparing NGTS-21b with currently known transiting hot Jupiters with similar equilibrium temperatures, it is found to have one of the largest measured radii despite its large mass. Inflation-free planetary structure models suggest the planet's atmosphere is inflated by ∼21 per cent, while inflationary models predict a radius consistent with observations, thus pointing to stellar irradiation as the probable origin of NGTS-21b's radius inflation. Additionally, NGTS-21b's bulk density (1.25 ± 0.15 g cm^{-3}) is also amongst the largest within the population of metal-poor giant hosts ([Fe/H] < 0.0), helping to reveal a falling upper boundary in metallicity–planet density parameter space that is in concordance with core accretion formation models. The discovery of rare planetary systems such as NGTS-21 greatly contributes towards better constraints being placed on the formation and evolution mechanisms of massive planets orbiting low-mass stars.

Key words: techniques: photometric – techniques: radial velocities – planets and satellites: detection – planets and satellites: fundamental parameters – planets and satellites: general – stars: general.

1 INTRODUCTION

The increasing number of planet discoveries has allowed us to classify exoplanets into distinct populations such as hot Jupiters (e.g. 51Peg b, Mayor & Queloz, 1995; NGTS-2, Raynard et al., 2018), which are planets with orbital period $P < 10$ d, and masses between 1–13 $M_{\rm J}$, ultrashort period (USP) planets, characterized by their P <1 d orbit (e.g. Kepler-10b, Batalha et al. 2011), Neptune desert planets (e.g. LTT9779b, Jenkins 2019), with masses and periods about 10–20$M_{\oplus}$ and $P < 4$ d, respectively, and super-Earths (e.g. Trappist-1, Gillon et al. 2017), with M <10$M_{\oplus}$. Amongst all planet populations, the hot and ultrahot giant planets are the most likely to be detected given their relative proximity to the host star, which maximizes the transit probability function and radial-velocity (RV) amplitudes. However, although giant planets are easily identified, observations show that their occurrence rates ($f_{\rm p}$) around solar-type stars are about 10 per cent (Cumming et al. 2008; Hsu et al. 2019), from which only ∼1 per cent are hot Jupiters (Wright et al. 2012), whereas for low-mass stars, Jovian planets are even less common (Johnson et al. 2007; Bonfils et al. 2013).

Another key discovery that was made relatively early in the history of exoplanet studies, was the correlation between giant planets $f_{\rm p}$ with stellar metallicities ([Fe/H]) (Gonzalez 1997; Santos, Israelian & Mayor 2001; Fischer & Valenti 2005; Osborn & Bayliss 2020), where not only such planets preferentially form around metal-rich stars but an increase in metallicity leads to a higher giant planet occurrence rates (Jenkins et al. 2017; Buchhave et al. 2018; Barbato et al. 2019). However, although the fraction of giant planets orbiting metal-poor stars ([Fe/H] < 0.0 dex) is significantly lower than their more metal-rich counterparts, the fraction is far from zero. In fact, a number of gas giants have been found orbiting stars with metallicities down towards an [Fe/H] of −0.5 dex. Mortier et al. (2012) found that the fraction of gas giants orbiting stars in the metallicity range −0.7–0.0 is actually ∼4 per cent, yet the hot Jupiters have a fraction below 1 per cent.

The stellar mass also plays an important role in the types of planets that can be formed orbiting a specific type of star. Johnson et al. (2010) found that higher mass stars tend to host more gas giant planets. This result has been confirmed by other works (Reffert et al.

★ E-mail: douglasalvesastro12@gmail.com (DRA); james.jenkins@mail.udp.cl (JSJ)

2015; Jones et al. 2016), likely being explained by the relationship between host star mass and disc mass, whereby as the stellar-mass decreases, and hence the disc mass decreases, there is less and less material with which to quickly form a giant planet before the disc disperses. These results imply that metal-poor and low-mass stars should be relatively devoid of gas giant planets, particularly the short-period hot Jupiter population.

1.1 The Next Generation Transit Survey

The Next Generation Transit Survey (NGTS; Chazelas et al. 2012; McCormac et al. 2017; Wheatley et al. 2018) is a collection of 12 telescopes operating from the ESO Paranal Observatory in Chile, with the goal of detecting new transiting planetary systems. Each telescope has a diameter of 0.2 m, and with individual fields of view of 8 deg^2, a combined wide field of 96 deg^2 can be obtained. Detectors are 2×2 K^2 pixels, with individual pixels measuring 13.5 μm, which corresponds to an on-sky size of 4.97 arcsec, thus providing high-sensitivity images over a wavelength domain between 520 and 890 nm. This combination allows 150 ppm photometry to be obtained on bright stars ($V < 10$ mag) for multicamera observations, while for single telescope mode at 30-min cadence, a precision of 400 ppm is achievable (Bayliss et al. 2022). The project has been operational since February 2016, and over the past 6 yr has so far acquired over 300 billion measurements of over 30 million stars. Within this treasure trove of data, the NGTS has discovered 19 new planetary systems (e.g. Bayliss et al. 2018; Bryant et al. 2020; Tilbrook et al. 2021), with more yet to be confirmed. A few of the highlights include the discovery of the Neptune desert planet NGTS-4b (West et al. 2019), an ultra short-period Jupiter NGTS-6b (Vines et al. 2019), and the shortest period hot Jupiter NGTS-10b around a K5V star (McCormac et al. 2020). Here, we add to the success of this project by announcing the discovery of a new, massive hot Jupiter orbiting a low-mass star, NGTS-21b.

The manuscript is organized as follows, in Section 2, we present the photometry extraction from NGTS, TESS, and SAAO light curve and HARPS spectroscopic follow-up. Section 3 describes the data analysis, where we extract stellar parameters (Section 3.1), assess TESS light-curves dilution (Section 3.2), and perform a global modelling to derive the planetary properties (Section 3.3). Stellar rotation period as well as transit-timing variation (TTV) were probed in Sections 3.4 and 3.5, respectively. Finally, we discuss our results in Section 4 and set out the conclusions in Section 5.

2 OBSERVATIONS

Here, we describe the observation data reductions that led to the discovery of NGTS-21b ; Table 1 shows a portion of the photometry for guidance.

2.1 NGTS photometry

NGTS-21 was observed during the 2018 campaign from March 24 to November 7, where 9157 images were obtained during 150 nights, with 10 s exposure time per frame. Prior to aperture photometry extraction with CASUTOOLS[1] package, nightly trends such as atmospheric extinction were corrected for with an adapted version of the SysRem algorithm (Tamuz, Mazeh & Zucker 2005). Transit searches were carried out with our implementation of the box least-squares (BLS) fitting algorithm (Kovács, Zucker & Mazeh 2002; Collier Cameron et al. 2006) ORION code, where a total of 25 transits were detected, of which 13 were full transits. A strong signal was detected at 1.543 d, and a validation process began in order to either confirm the signal as a likely transiting hot Jupiter or reject it as a false-positive detection. For example, background eclipsing binaries, where consecutive transits show odd–even and/or V-shaped transits. NGTS-21 passed every validation step, and therefore further photometry and RV follow-up were obtained. Fig. 1 shows the NGTS detection light curve wrapped around the best-fitting period 1.543 3897 ± 0.000 0016 d computed from the global modelling

[1] http://casu.ast.cam.ac.uk/surveys-projects/software-release

Table 1. NGTS, TESS and SAAO photometry for NGTS-21. The full Table is available in a machine-readable format from the online journal. A portion is shown here for guidance.

Time (BJD$_{TDB}$-2457000)	Flux (normalized)	Flux error	Instrument
–	–	–	–
1203.89922322	1.0029	0.0137	NGTS
1203.90264915	1.0172	0.0120	NGTS
1203.904506795	1.0801	0.0383	NGTS
1204.872232445	0.9932	0.0083	NGTS
1204.87575096	0.9935	0.0141	NGTS
1204.87920004	0.9812	0.0122	NGTS
1204.88266068	1.0091	0.0096	NGTS
–	–	–	–
2051.58581	0.9994	0.0109	TESS
2051.59276	0.9968	0.0109	TESS
2051.5997	0.9674	0.0110	TESS
2051.60665	0.9980	0.0110	TESS
–	–	–	–
2051.43517437	0.9811	0.0083	SAAO
2051.4358689	0.9866	0.0083	SAAO
2051.43656342	0.9916	0.0083	SAAO
2051.43725795	0.9925	0.0084	SAAO
–	–	–	–

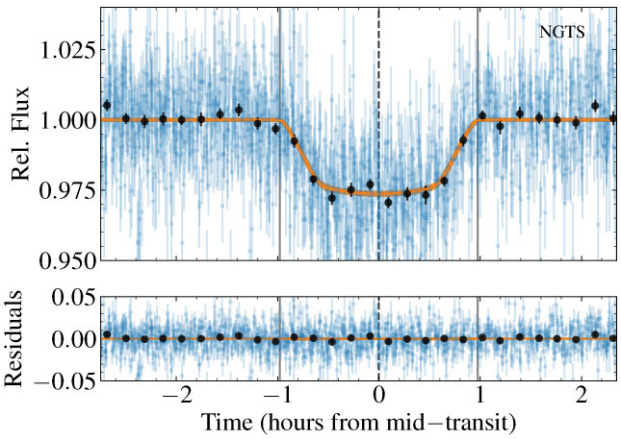

Figure 1. Top panel: NGTS detrended light-curve phase-folded to the best-fitting period listed in Table 4 and zoomed to show the transit event. Blue and black circles correspond to modelled photometric data and 11-min binned data with the associated photon noise error. The orange line and shaded region show the median transit model and its 1σ confidence interval. Solid grey vertical lines indicate the start of transit ingress (T_1) and end of egress (T_4). Dashed grey vertical line represents the transit centre (T_c). Bottom panel: residuals to the best-fitting model.

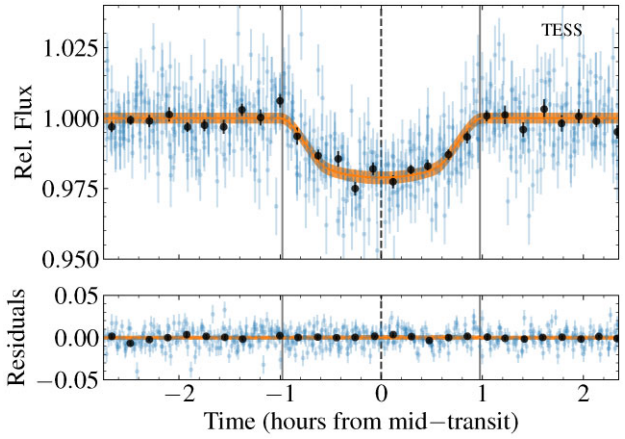

Figure 2. Phase-folded TESS detrended light curve. Coloured are labelled as in Fig. 1.

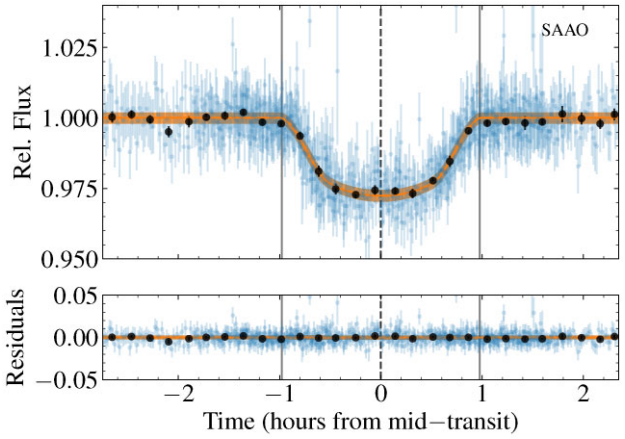

Figure 3. Phase-folded SAAO of the three detrended light curves. Coloured are labelled as in Fig. 1.

(Section 3.3). For a detailed description of the NGTS mission, data reduction, and acquisition, we refer the reader to Wheatley et al. (2018).

2.2 TESS photometry

The Transiting Exoplanet Survey Satellite (TESS; Ricker et al. 2015) observed NGTS-21 in sector 1 on universal time (UT) 2018 July 26 and sector 27 on UT 2020-7-5, with cadences of 30 and 10 min, respectively. Full Frame Images (FFIs) have been downloaded using the python astroquery module (Ginsburg et al. 2019) to query the TESSCut service (Brasseur et al. 2019). For each sector, a master image was calculated and used to both determine the star aperture and identify pixels for background correction, thus estimating NGTS-21 brightness for each image. Fig. 2 shows the detrended phase-folded light curve, median, and 1σ best-fitting model from Section 3.3.

2.3 SAAO photometry

Follow-up photometry of NGTS-21 was obtained with the South African Astronomical Observatory (SAAO) 1-m telescope equipped with the Sutherland High-Speed Optical Camera (SHOC; Coppejans et al. 2013). The star was observed three times, on the nights of 2020 June 19, July 20 and July 23. All observations were taken in *V* band with 60 s of exposure times.

The data were reduced using the `safphot`,[2] a custom python package for the reduction of SAAO photometric data. Standard flat-field and bias corrections were applied by `safphot`, which then utilizes the `sep` package (Barbary 2016) to extract aperture photometry for both the NGTS-21 and nearby comparison stars with which to perform differential photometry. `sep` also measured and subtracted the sky background, while masking the stars in the image and adopting box sizes and filter widths that minimized residuals across the frame. Two nearby, bright comparison stars were used to perform differential photometry, with aperture sizes ranging between 4.4 and 5.9 pixels for the target dependent on the seeing level.

The July 2020 observations both captured complete transits of NGTS-21b, whereas the 2020 June 19 was affected by clouds during mid-transit, thus leading to gaps at that portion. However, since both ingress and egress were observed, the data was used in the global modelling in Section 3.3, where Fig. 3 shows the phase-folded SAAO follow-up light curve.

[2]https://github.com/apchsh/SAFPhot

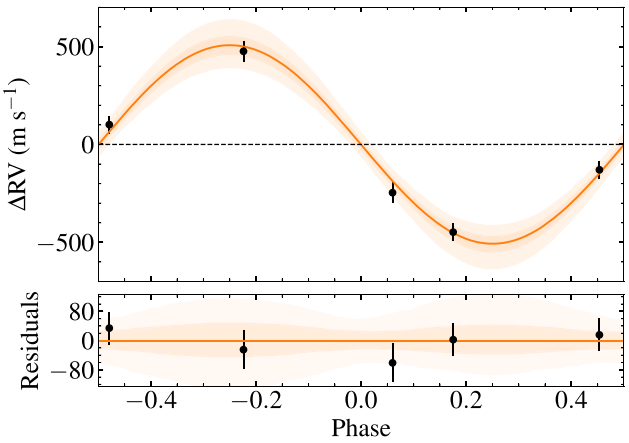

Figure 4. Top panel: Phase-folded HARPS RV shown in black, with its 1σ and 2σ confidence intervals in shades of orange. Bottom panel: residuals to the best fitting with $\mathrm{RMS_{RV}} = 33.75$ ms^{-1}.

2.4 Spectroscopic follow up

Five high-resolution spectra for NGTS-21 were obtained during UT 2021 July 2021 and 2021 2021 September 07 under the HARPS prog ID (Wheatley 0105.C-0773) on the ESO 3.6 m (Mayor et al. 2003) telescope at the la silla observatory in Chile. Due to the apparent faintness of the star and large expected RV amplitude, we used HARPS in the high-efficiency mode (EGGS), which trades resolution for high throughput. The EGGS science fibre is 1.4 arcsec when projected on-sky, which with exposure times of 2400–2700 s, we achieved a signal-to-noise ratio (S/N) of 4–5 per pixel at 5500 Å. The RV measurements were computed with the standard HARPS pipeline using the following binary masks for the cross-correlation: G2, K5, K0, and M4, where agreement was found amongst the RVs estimated with these binary masks. Therefore, given NGTS-21 spectral type, we adopted the RV data estimated with the binary K5 mask, which is shown, accompanied by the best-fitting Keplerian model, in Fig. 4 as well as in Table 2 with additional diagnostics data.

Since stellar activity has long been recognized to mimic planetary signals, we investigated whether correlations are present between

Table 2. HARPS follow-up radial velocities for NGTS-21.

BJD_{TDB} −2457000	RV ($m\,s^{-1}$)	RV error ($m\,s^{-1}$)	FWHM ($m\,s^{-1}$)	BIS ($m\,s^{-1}$)
2411.818920	13851	27	7283	110
2428.692090	13620	27	7390	009
2460.673898	13302	27	7154	099
2463.582604	13503	39	7198	148
2464.688277	14226	41	7224	123

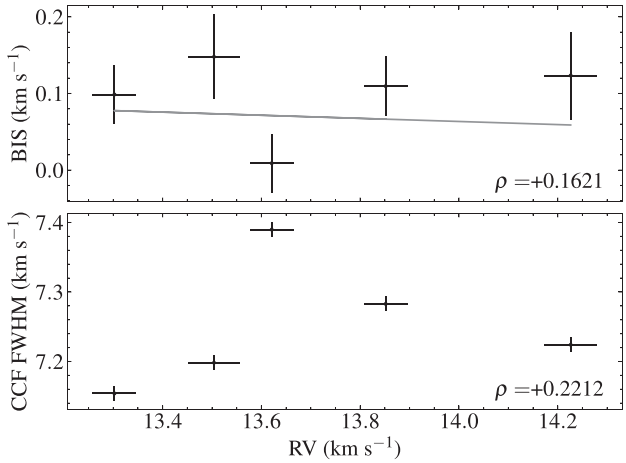

Figure 5. Top panel: RV versus bisector span measurement with a best-fitting linear model shown as grey solid line. The Pearson r coefficient supports no significant correlation between data sets, with ρ shown at the lower right-hand panel. Bottom panel: RV against CCF full width at half maxima.

activity diagnosis parameters to rule out the possibility of a false-positive signal. Fig. 5 upper left-hand panel shows the RV measurements versus bisector velocity span (BIS) of the cross-correlation function (CCF) with a best-fitting linear model. A Pearson r coefficient, which measures the correlation between data sets, approaches zero ($\rho = +0.1621$), thus pointing to negligible correlation between the RVs and BIS. The full width at half-maxima (FWHM) is also shown in the bottom panel indicating no trend between RV and CCF−FWHM. Finally, the light curves low rotational modulation and lack of observable flares in the light curves are in accordance with a moderately quiet star, thus supporting the RV and transit detected signal as coming from NGTS-21b.

Due to variations of up to 236 ms^{-1} in the CCF−FWHM (Fig. 5), likely caused by the very low S/N, we performed modelling tests based on Section 3.3 to investigate whether the removal of the second HARPS spectrum listed in Table 2 would impact the posterior distributions derived when the entire RV data is included in the model. Since the tests yielded posterior distributions that are in strong statistical agreement, we included every RV measurement while building our global model in Section 3.3.

3 DATA ANALYSIS

3.1 Stellar properties

NGTS-21 properties were independently derived using the packages, spectroscopic parameters and atmospheric chemistries of stars (`SPECIES`[3]; Soto & Jenkins 2018) and the spectral energy distribution (SED) Bayesian model averaging fitter (`ARIADNE`;[4] Vines & Jenkins 2022).

`SPECIES` estimates atmospheric parameters such as effective temperature ($T_{\rm eff}$), [Fe/H], surface gravity ($\log g$), and microturbulence velocity (ξ_t) from high-resolution spectra. First, `SPECIES` computes the equivalent widths (W) of Fe I and Fe II lines with the `ARES` code (Sousa et al. 2007). An appropriate atmospheric grid of models computed from interpolating ATLAS9 (Castelli & Kurucz 2004) atmosphere model as well as W are handed to MOOG (Sneden 1973), which solves the radiative transfer equation (RTE) while measuring the correlation between Fe line abundances as a function of excitation potential and W, assuming local thermodynamic equilibrium (LTE). While solving the RTE, the correct atmospheric parameters are determined through an iterative process carried out until no correlation is found between the iron abundance with the excitation potential, and with the reduced equivalent width (W/λ). The Mass, radius and age are obtained from the `isochrone` package (Morton 2015) by interpolating through a grid of MIST (Dotter 2016) evolutionary tracks with $T_{\rm eff}$, [Fe/H], $\log g$ priors previously derived as well as parallax, photometry in several bands, and proper motions. Nested sampling (Feroz, Hobson & Bridges 2009) is used to estimate posterior distributions for $M_{\rm s}, R_{\rm s}$, and age. Rotation and macro turbulent velocities are calculated from temperature calibrators and fitting the absorption lines of observed spectra with synthetic line profiles. From our analysis using `SPECIES`, we derived the following stellar properties with their 1σ confidence interval, $T_{\rm eff} = 4746 \pm 300$ K, [Fe/H] $= -0.26 \pm 0.09$ dex, $\log {\rm g} = 4.57 \pm 0.45$, Age $= 11.72^{+1.28}_{-2.36}$ Gyr, $M_{\rm s} = 0.75 \pm 0.01\,{\rm M}_{\odot}$, and $R_{\rm s} = 0.74 \pm 0.01\,R_{\odot}$. Chemical abundances and *vsini* were not extracted due to the low-S/N achieved at this faint regime ($V = 15.6$).

We have also estimated NGTS-21 parameters using the `ARIADNE` python package (Vines & Jenkins 2022), which is an automated code that extract stellar parameters by fitting archival photometry to different stellar atmosphere models using Nested Sampling through `DYNESTY` (Speagle 2020). The `SPECIES` derived stellar properties $T_{\rm eff}$, $\log g$, and [Fe/H] as well as archival photometric data were used as `ARIADNE` input to fit the SED using different models (Fig. 6). These models were convolved with several filter response functions (see available SED models in Vines & Jenkins 2022), where synthetic fluxes scaled by $(R/D)^2$ were estimated from interpolating through the model grids, which are functions of $T_{\rm eff}$, $\log g$, [Fe/H], and V-band extinction ($A_{\rm V}$). An excess noise parameter is modelled for each photometric measurement to account for underestimated uncertainties. The final stellar parameters are derived from the averaged posterior distributions from the Phoenix V2 (Husser et al. 2013), BT-Settl (Hauschildt, Allard & Baron 1999; Allard, Homeier & Freytag 2012), Castelli & Kurucz (2004), and Kurucz (1993) SED models, weighted by their respective Bayesian evidence estimates. `ARIADNE` parameters $T_{\rm eff}$, $\log g$, [Fe/H] as well as additional quantities such as distance, stellar radius, and $A_{\rm V}$ were used to derive stellar age, mass and the equal evolutionary points from the `isochrone` package. Table 3 shows the adopted stellar properties from `ARIADNE`, which due to its Bayesian averaging method computed precise stellar parameters, particularly the $R_{\rm s}$ and $T_{\rm eff}$, which were key to inform the global modelling of NGTS-21b (see Section 3.3).

For consistency, we compared the GAIA DR3 stellar parameters $T_{\rm eff} = 4665^{+15}_{-24}$ K, log g $= 4.53^{+0.03}_{-0.07}$ dex, $R_{\rm s} = 0.83^{+0.12}_{-0.04}\,R_{\odot}$, and

[3] github.com/msotov/SPECIES
[4] https://github.com/jvines/astroARIADNE

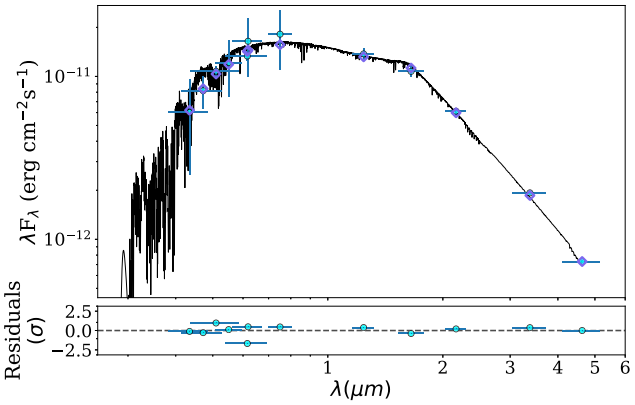

Figure 6. Top panel: The best-fitting SED (black line) based on Castelli & Kurucz (2004) given the NGTS-21 photometric data (cyan points) and their respective bandwidths shown as horizontal error bars. Purple diamonds represent the synthetic magnitudes centred at the wavelengths of the photometric data from Table 3. Bottom panel: residuals to the best fit in σ units.

Table 3. Stellar Properties for NGTS-21.

Property	Value	Source
Astrometric Properties		
RA	$20^h45^m01^s.9941$	*GAIA*
Dec.	$-35°25'40''.2322$	*GAIA*
2MASS ID	J20450201–3525401	*2MASS*
TIC ID	441422655	*TIC*
GAIA DR3 ID		*GAIA*
	6779 308 394 419 726 848	
Parallax (mas)	1.71 ± 0.03	*GAIA*
μ_{RA} (mas y^{-1})	− 13.443 ± 0.031	*GAIA*
$\mu_{Dec.}$ (mas y^{-1})	− 7.834 ± 0.028	*GAIA*
Photometric properties		
V (mag)	15.621 ± 0.096	*APASS*
B (mag)	16.648 ± 0.107	*APASS*
g (mag)	16.108 ± 0.048	*APASS*
r (mag)	15.241 ± 0.076	*APASS*
i (mag)	14.856 ± 0.203	*APASS*
G (mag)	15.22400 ± 0.00041	*GAIA*
NGTS (mag)	14.82	This work
TESS (mag)	14.5499 ± 0.006	*TIC*
J (mag)	13.622 ± 0.027	*2MASS*
H (mag)	13.105 ± 0.028	*2MASS*
K (mag)	12.951 ± 0.029	*2MASS*
W1 (mag)	12.898 ± 0.024	*WISE*
W2 (mag)	12.969 ± 0.027	*WISE*
W3 (mag)	12.485 ± 0.515	*WISE*
Derived properties		
ρ_* (g cm^{-3})	1.62 ± 0.10	`Juliet`
γ_{RV} (km s^{-1})	13.75 ± 0.02	`Juliet`
P_{rot} (d)	17.89 ± 0.08	This work
T_{eff} (K)	4660 ± 41	`ARIADNE`
[Fe/H]	− 0.26 ± 0.07	`ARIADNE`
log g	4.63 ± 0.34	`ARIADNE`
Age (Gyr)	$10.02^{+3.29}_{-7.30}$	`ARIADNE`
$M_s(M_\odot)$	0.72 ± 0.04	`ARIADNE`
$R_s(R_\odot)$	0.86 ± 0.04	ARIADNE
Distance (pc)	$640.98^{+26.96}_{-23.59}$	`ARIADNE`

Notes. 2MASS (Skrutskie et al. 2006); *TIC* v8 (Stassun et al. 2018); *APASS* (Henden & Munari 2014); *WISE* (Wright et al. 2010); *Gaia* (Brown et al. 2021).

distance of 612^{+85}_{-27} pc, with both `SPECIES` and `ARIADNE`, and found the measurements to be in statistical agreement. The GAIA astrometric excess noise as well as the renormalized unit weight error are 0 and 1.005, respectively, which are consistent with NGTS-21 being a single-star system.

3.1.1 Age estimation

The age of stars are commonly estimated using grids of pre-computed stellar evolutionary models described by stellar physical properties (e.g. temperature, luminosity, metallicity, etc.) that are interpolated to fit a set of observed stellar parameters. Such evolutionary models could be rearranged to tracks of fixed ages, i.e, isochrones, from which stellar ages are estimated. However, the complexity and strong non-linearity of isochrones along with observational uncertainties make it difficult to precisely estimate stellar ages.

Although `ARIADNE` and `SPECIES` show consistent ages posteriors, the former gives a broader distribution than the latter. Therefore, we assessed NGTS-21 age based on gyrochronology models, which assume that stellar ages are a first-order function of the rotation period, thus relying on less assumptions compared to other age estimation methods. The gyrochronology models we used were based on Barnes (2007), Mamajek & Hillenbrand (2008), and Meibom, Mathieu & Stassun (2009), which point to an age between 1 and 4.5 Gyr for a rotation period (P_{rot}) of about 18 d (see Section 3.4 for the P_{rot} calculation). Additionally, we used the `stardate` (Angus et al. 2019) code, which combines the `isochrone` package with gyrochronology models, thus computing an age of $4.94^{+3.56}_{-2.59}$ Gyr. Since pure gyrochronology models as well as the joint analysis with isochrone fitting yield ages in statistical agreement with `ARIADNE`, we adopted the `ARIADNE` age of $10.0^{+3.29}_{-7.30}$ Gyr. Yet, NGTS-21 age lower end may be more likely given its moderately low activity supported by its lack of flares as well as measured rotational period and amplitude (Section 3.4).

Finally, we checked NGTS-21 spectrum for lithium lines, which due to its volatility with temperature, its abundance are depleted quickly in stellar atmospheres already in the first hundred million years of the star lifetime, hence the existence of photospheric Li is frequently associated to young stars (e.g. see Christensen-Dalsgaard & Aguirre 2018). Therefore, we searched for Li lines in the averaged spectra, particularly around the strong Li resonant doublet at 6708 Å, and found no evidence for Li lines, thus giving further constraints in NGTS-21 lower age limit (>50–100 Myr).

3.2 Assessment of TESS light-curve dilution

TESS light curves are very susceptible to dilution, particularly in crowded fields where several contaminants may be within a few arcseconds from the target star. Due to its large plate scale of 21 arcsec pixel^{-1}, nearby stars may fall inside the photometric aperture, thus causing blends that affect transit depth, which in turn underestimate fundamental planetary properties such as planet radius and bulk density. To account for this, we assess the level of contamination in TESS light curves by estimating the dilution factor (D) to be used as a prior in the global modelling.

A comparison between transit depths from the three missions shows that the planet-to-star radius ratio estimated from NGTS (0.161 ± 0.003) and SAAO (0.157 ± 0.003) are consistent, whilst TESS smaller ratio (0.138 ± 0.005) indicates a shallower transit depth likely caused by two stars in the photometric aperture (see Fig. 7). To estimate the dilution level, we used the `ARIADNE` code

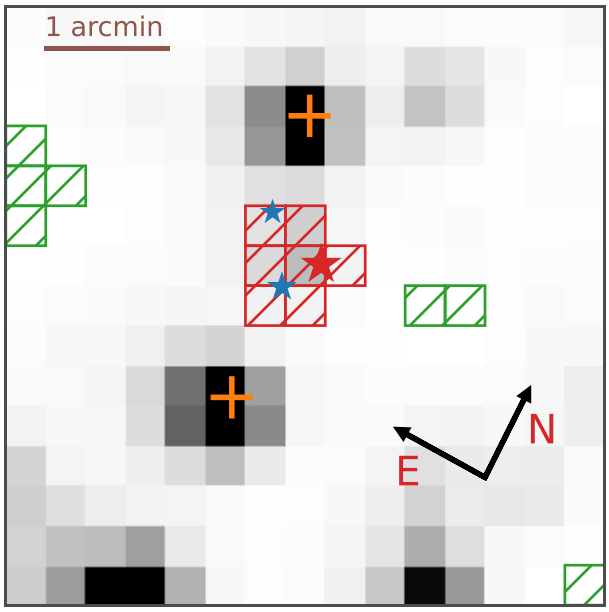

Figure 7. TESS Sector 1 Full-Frame Image cutout (15 x 15 pixels) centred at NGTS-21b (red star). Red squares represent the mask used for the photometry extraction, green squares are the pixels utilized to estimate the sky background brightness. Stars marked in blue represent TIC-441422661 with a V =18.2 (upper left-hand panel) and TIC-441422652 with V =17.3 (lower left-hand panel). Orange pluses show the brightest stars in the field, TIC-441422643 (V =13.4) and TIC-441422667 (V = 14) at the bottom left-hand panel and upper right-hand panel, respectively.

to compute the SED for NGTS-21 and the two contaminants, TIC-441422661 and TIC-441422652, which are 37.86 and 22.61 arcsec from NGTS-21, respectively. Synthetic fluxes were computed by `ARIADNE`, where a theoretical D ∼20.5 per cent in the TESS band, from equation (1), where $F_{\rm cont}$ and $F_{\rm target}$ represent the contaminant and target fluxes, respectively.

$$D = \sum_{cont} F_{\rm cont}/F_{\rm target}. \quad (1)$$

For consistency, we have also estimated the dilution directly from the phase-folded light curves transit depths offset between TESS and NGTS. We assumed no dilution for the later since the contaminants light contribution inside the NGTS apertures are, if any, negligible due to their relative distances (>22.6 arcsec) to NGTS-21 as well as their faint magnitudes ($V >$ 17 mag). We found a dilution of ∼26.5 per cent, which is 6 per cent larger than the predicted dilution from the SED fitting. This may be due to some fractional flux entering the aperture coming from the two brighter stars in Fig. 7, which are flagged with oranges crosses. Upon running several tests by varying the dilution prior distribution, we chose a Gaussian prior centred at $\mu = 28$ per cent and $\sigma = 10$ per cent for the global modelling (see Section 3.3), thus resulting in a posterior dilution D $=27.5^{+6.1}_{-5.9}$ per cent.

3.3 Global modelling

We performed a joint RV and photometric analysis with the `Juliet` (Espinoza, Kossakowski & Brahm 2019) python package, which is a versatile code wrapped around the `Batman` (Kreidberg 2015) for light-curve modelling and `radvel` (Fulton et al. 2018) for RV analysis. Our data set consists of five HARPS RVs and a total of 13 616 photometric data points from NGTS, TESS, and SAAO.

Since each instrument has its own precision, and work under distinct environmental conditions, each data set encapsulates noise differently, thus requiring a proper modelling so that planetary properties are optimally derived. For that reason, we included Gaussian processes (GP) in the noise model to account for correlated noise in the light curves, where each instrument was modelled by an approximate Matern Kernel. No GP was added to the Keplerian part of the global model due to the risk of overfitting caused by the low number of RV points. Although a global GP kernel is preferred for a proper modelling of stellar activity, we use a multi-instrument GP approach because NGTS-21 presents moderately low activity compared to instrumental systematic, particularly the TESS light curve, which shows the largest correlated noise (see Fig. 8a) amongst the data set.

As discussed in Section 3.2, TESS photometry is diluted by at least two contaminants, therefore a dilution normal prior ($\mathcal{N}(0.78, 0.1^2)$) was added specifically for this instrument,[5] whereas NGTS and SAAO light curves had dilution factors set to undiluted.

For the limb darkening, we used the approach described in Kipping (2013), where a quadratic parametrization with q_1 and q_2 using uniform priors $\mathcal{U}(0, 1)$ were introduced for each instrument. The eccentricity e was fixed to zero due to the small number of RV points. Yet, this assumption is supported by (1) observations of short-period HJs ($P <$ 4 d), which are frequently found in circular orbits, and (2) NGTS-21b tidal circularization time-scale τ of ∼1–11 Myr, which was computed with equation (3) from Adams & Laughlin (2006), assuming a tidal quality factor $Q_{\rm p}$ of 10^5-10^6. Such a short τ compared to the planetary system lifetime quickly circularised the planet's orbit through planet–star dynamical interactions. Although a circular orbit was adopted, we ran tests to investigate whether a model with free e would be preferred based on the Bayesian information criterion (BIC). The BIC is a model selection tool useful to test whether an increase in likelihood justifies the addition of new parameters in the tested model, which in turn, could lead to overfitting. The runs with non-circular orbits provided an upper limit of $e < 0.12$ at 1σ and a BIC of 27.1, while the run with circular orbit yielded a BIC of 25.5. Therefore, given that models with lower BIC values are favoured, the NGTS-21 global modelling with a circular orbit was preferred.

The RV part of the global model includes a Keplerian, a systemic RV term ($\gamma_{\rm RV}$) and a white-noise term to account for stellar jitter. Finally, due to the high dimension of the parameter space, we used the dynamic nested sampling algorithm (Higson et al. 2019) through `DYNESTY` with 1000 live points.

3.4 Stellar rotation from NGTS data

The rotation period of stars can be measured by modelling the photometric brightness variation caused by star spots coming in and out of sight as stars spin. Thanks to several ground- and space-based missions, $P_{\rm rot}$ measurements have been extracted for thousands of stars of distinct spectral types (McQuillan, Mazeh & Aigrain 2014; Martins et al. 2020; Briegal et al. 2022b), thus helping set constraints on the dominant mechanisms driving stellar angular momentum evolution (Kawaler 1988; Bouvier et al. 2014). Moreover, rotation periods are widely used to calibrate gyrochronology models (Angus

[5] `Juliet` dilution definition is given by $\frac{1}{1+D}$, with D from equation (1).

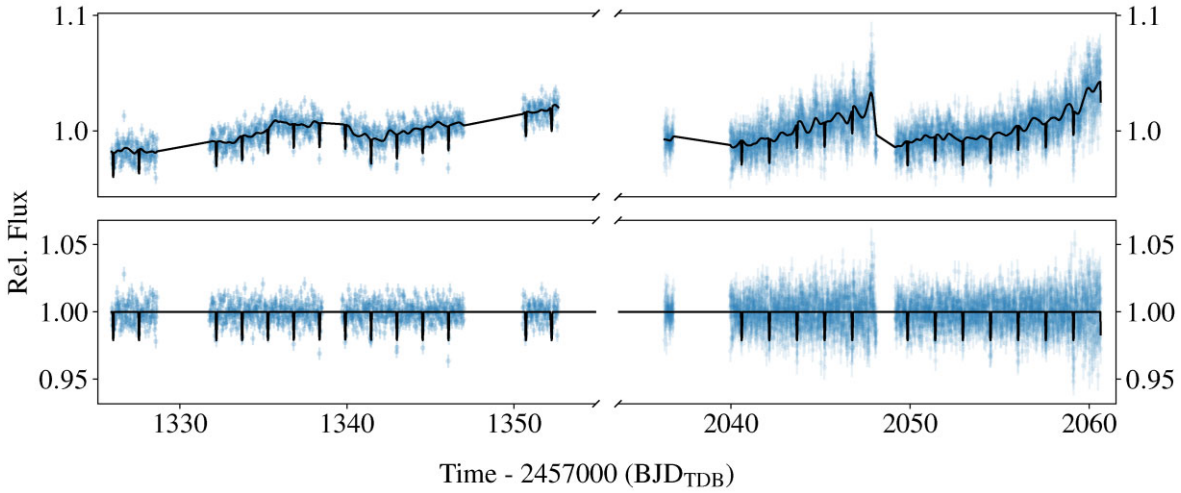

Figure 8. Top panel: TESS light curve extracted from FFIs showing moderate systematic (in blue), and its joint transit and GP best-fitting median model in black. Left and right *y*-axis correspond to 30- and 10-min cadence light curves from Sector 1 and 27, respectively. Bottom panel: detrended light curve in blue with its transit-only best-fitting model in black.

et al. 2019), which, in turn, are used to infer stellar ages as a first-order function of $P_{\rm rot}$, yet limitations exist (Barnes 2007; Epstein & Pinsonneault 2013).

We extracted NGTS-21 rotation period with the Lomb–Scargle (LS) periodogram (Rebull et al. 2016; VanderPlas 2018) as well as autocorrelation functions (ACF) methods (Angus et al. 2018). Each technique has its own assumptions, advantages, and limitations, i.e, while the LS method assumes a sinusoidal function to model the rotation signal, thus best suited for data sets presenting stable oscillations, the ACF technique is a more flexible method that measures the degree of similarity between different parts of the data set (see, Gillen et al. 2020).

Prior to the period search, we masked the transits and binned the data to 30-m cadence. Both LS and ACF methods are applied to the data set, which detect rotation periods whose difference is of $\delta P_{\rm rot}$ = 0.1 d (Fig. 9). Since neither LS nor ACF techniques provide a confidence interval, a bootstrap approach was used to draw 15000 sample from the data with replacement. For each sample we fitted a sine model and compute the rotation period from the LS periodogram, thus generating distributions for both $P_{\rm rot}$ and amplitude ($A_{\rm rot}$), where the median and 1σ intervals give $P_{\rm rot}$ = 17.89 ± 0.1 d and $A_{\rm rot}$ = 10 ± 1 ppt. In order to provide further confidence on our $P_{\rm rot}$ estimation, we attempted to measure the activity index $\log_{10}R_{HK}$ and projected rotational velocity vsini, yet we were unable to estimate such parameters due to the spectrum low (<10) S/N. Fig. 9 (top panel) shows the phase-folded light curve to the period at maximum power of the LS periodogram (centre panel) from one bootstrap realization with its corresponding sinusoidal model, while the rotation period from the ACF (bottom panel) was computed with the `astroML` package based on the Edelson and Krolik method (Edelson & Krolik 1988), where we adjusted an underdamped Simple Harmonic Oscillator (uSHO) to the data in order to extract the period. The LS method is available through the `astropy` package based on VanderPlas & Ivezic (2015).

Finally, we visually checked the periods presenting moderately high LS power, and ruled out the ones below and near one day, which are likely associated to either instrumental noise or poor observing conditions. Yet, the ∼14.2 d signal near the rotation period cannot be associated to neither half the Lunar cycle of 14.8 d nor other non-astrophysical signals. Therefore, we followed the same procedure

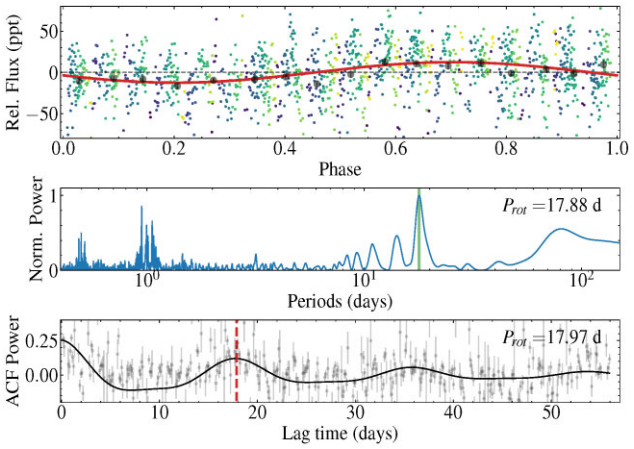

Figure 9. Top panel: NGTS light curve wrapped around the best-fitting LS period, where blue to green colors represent beginning to end of observations. Red line shows a sinusoidal model with amplitude $11.4^{+1.4}_{-1.6}$ ppt. Middle panel: The LS periodogram of the NGTS-21b photometric data. The green bar centred at the highest peak displays the rotational period $P_{\rm rot} = 17.89 \pm 0.08$ d. Bottom panel: Lag time as a function of ACF power. Red vertical dashed line marks the first highest autocorrelation period at lag time 17.97 d, matching NGTS-21 rotation period.

described above to model the 14.2 d signal, and found the best-fitting period and amplitude of 14.18 ± 0.13 d and 9.27 ± 0.98 ppt, respectively, and associate it to a possible NGTS-21 differential rotation. The stellar rotation period we derived was independently confirmed with the `RoTo`[6] code (Briegal et al. 2022a), which extracts stellar rotation periods automatically using LS, generalized ACF and GP, thus providing further confidence on our reported measurement.

3.5 TTV analysis

The TTV method (Agol et al. 2005) was responsible for the validation of several multiplanet systems around faint stars from the Kepler

[6]https://github.com/joshbriegal/roto

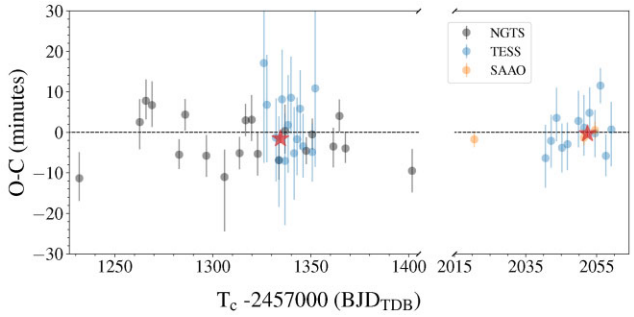

Figure 10. NGTS-21b computed transit-timing variation. The zero dashed line indicates no deviation from the linear ephemeris model. Red stars represent the left and right portion of data sets average, with inverse variances as weights. 1. A table is available in a machine-readable format from the online journal.

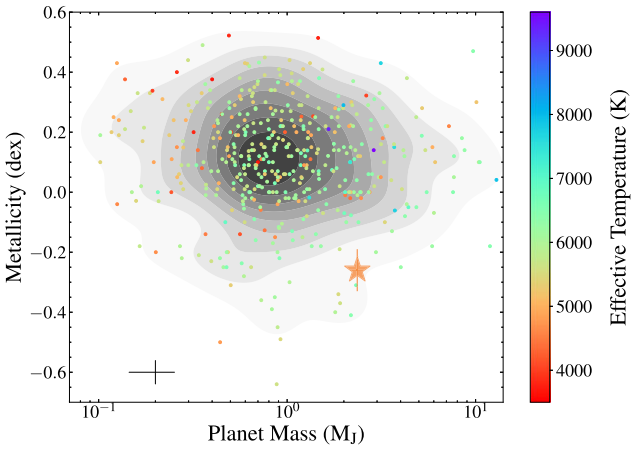

Figure 11. Transiting HJs planet mass against stellar metallicity. Stars are colour-coded by their effective temperature, and NGTS-21b is represented as an orange star symbol towards the bottom right-hand side of the plot. Dark to light shades of grey represent high to low planet number density, and black cross at the bottom left-hand corner represents the standard deviation of planet mass and [Fe/H] uncertainties.

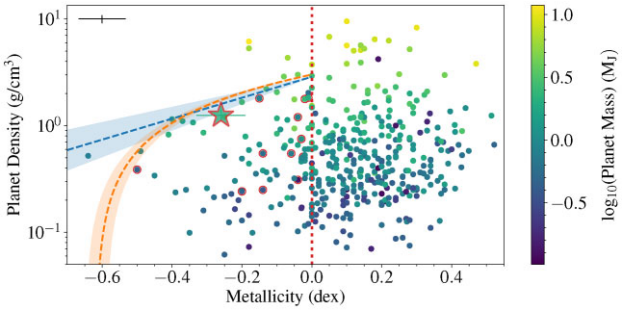

Figure 12. Stellar metallicity versus planet bulk density colour-coded by the logarithm of planet mass. Red open circles show metal-poor ([Fe/H] < 0) K dwarf stars ($T_{\rm eff} = 3900-5200$ K). The NGTS-21 system is indicated by the light green star at the upper left-hand panel from centre, while the black cross at the top left-hand corner represents the standard deviation of HJs uncertainties. Blue and orange dashed lines represent empirical exponential and linear models with shaded regions displaying their 1-σ confidence intervals, respectively. The zero metallicity border is shown as red vertical dashed line.

mission (Cochran et al. 2011; Steffen et al. 2012b; Gillon et al. 2017). Since the majority of Kepler stars were faint, the RV method lacked enough precision to confirm the majority of the transits as bonafide planets, although a few had RV detections (Barros et al. 2014; Almenara et al. 2018). Therefore, the TTV method became key to determine planetary masses/eccentricities for faint multiplanet systems (Lithwick, Xie & Wu 2012). Moreover, extensive TTV/RV searches for hot Jupiter companions supported the hypothesis that such massive planets are not part of multiplanet system (Steffen et al. 2012a; Holczer et al. 2016), thus setting major constraints on giant planets orbital evolution.

The TTV method consists of measuring the difference between each mid-transit $T_{\rm n}$ from the expected transit time computed with a linear ephemeris model given by $T_{\rm n} = T_0 + n \times P$, where n and P are the transit number and period, respectively. Deviation from the linear model is frequently associated to dynamical interactions, with the most common cases being planets near mean-motion resonances (e.g. Bryant et al. 2021) and planet–star tidal interaction leading to orbital decay (Yee et al. 2019).

NGTS-21b observed transit times as well as the linear fit were done with `Juliet` while holding all parameters to the posterior median from Table 4 except for the set of $T_{\rm n}$, which was given a normal prior $\mathcal{N}(T_n, 0.1^2)$. Fig. 10 shows the modelled observed transit times subtracted from the best-fitting linear model $T_{\rm n} = (2458\,214.8890 \pm 0.0012) + n \times (1.543\,3891 \pm 0.000\,0033)$, which indicates an agreement between observed transits and the model.

4 DISCUSSION

Our data analysis (Section 3) reveals what is the first NGTS discovery of a rare planetary system composed of a massive planet hosted by a relatively metal-poor star. These properties place NGTS-21 at a heavily underpopulated region of the $M_{\rm J}$ versus [Fe/H] parameter space (Fig. 11), and the only massive giant hosted by a K dwarf at that [Fe/H], thus making NGTS-21 a unique system.

4.1 The stellar metallicity versus bulk density plane

Fig. 12 compares host star metallicity with planetary bulk density ($\rho_{\rm b}$) for a well-studied population of HJs from the TEPCat catalogue (Southworth 2011), all colour-coded by planetary mass. Our analysis shows that NGTS-21b is relatively dense (1.25 ± 0.15 g cm^{-3}) when compared to other HJs orbiting K dwarf metal-poor stars, and one of the densest amongst metal-poor hosts below [Fe/H] < -0.2. Moreover, a clear upper boundary is observed, with planets $\rho_{\rm b}$ decreasing as an inverse function of stellar metallicity. Such a trend is in agreement with core-accretion models, whereby HJs formed in low-metallicity environments would have smaller cores, and consequently lower bulk densities, which descends as even less metal content is present. Two empirical models were adjusted as an approximation to match this upper boundary reflecting the possible correlation between [Fe/H] and $\rho_{\rm b}$. The model in blue represents an exponential of the form $\rho_{\rm b} = a e^{b[{\rm Fe/H}]}$, with a and b given by 2.9 ± 0.1 and 2.3 ± 0.6, while the linear model in orange was defined as $\rho_{\rm b} = c[{\rm Fe/H}] + d$, with c and d given by 4.9 ± 0.2 and 3.01 ± 0.03. Although we used empirical models to derive an upper boundary for HJs bulk densities, a larger sample of transiting HJs hosted by metal-poor stars, as well as a proper physical model to describe planet formation as a function of protoplanetary disc metallicity, are necessary to claim such correlation. Finally, a metal-poor gap may exist in the parameter space, with two classes of HJs orbiting metal-poor stars, the dominant population being low density

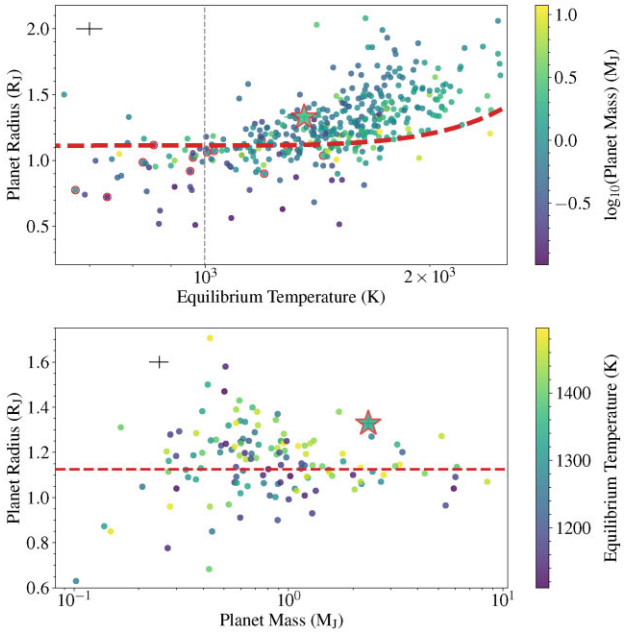

Figure 13. Top panel: equilibrium temperature versus planet radius colour-coded by the logarithm of planet mass. Red dashed line represents an inflation-free model for a HJ evolved to 4.5 Gyr with a H/He composition adapted from Thorngren & Fortney (2018). NGTS-21b is displayed by the light green star above the model and near the image centre. Black cross at the top left-hand corner represents the HJs parameters uncertainties standard deviation, and red open circles marks metal-poor K dwarf stars. Bottom panel: M_p versus R_p colour coded by T_{eq} showing HJs from the top figure with T_{eq} between 1100 and 1500 K. Red dashed line shows expected radius of $1.125R_J$ from the same inflation-free model at NGTS-21b T_{eq}.

and metal-poor HJs, and a less crowded population of higher density HJs, possibly large core-hosting planets. In order to confirm such a hypothesis, more transiting HJ planets are required within the metal-poor parameter space, particularly dense HJs, such that statistical samples can be drawn to test the reality of the gap.

4.2 Radius inflation

Several studies point to a high incident stellar flux as being the probable mechanism responsible for the HJs radius inflation, where energy is deposited into the planet interior, thus leading to an increase in radius. Demory & Seager (2011) and Miller & Fortney (2011) show that the physical mechanisms driving the radius anomaly operates above an incidence flux throughput of $\sim 2 \times 10^5$ Wm^{-2} while Thorngren & Fortney (2018) performed statistical analysis based on planetary thermal evolution models on a sample of 281 HJs, and showed the necessary conversion of incident flux to internal heating required to reproduce HJs observed radii peak at equilibrium temperature (T_{eq}) $\sim$1500 K. Hartman et al. (2016) show that HJ radii grows as a function of main-sequence stars fractional ages, i.e. as stars age on the main sequence, they brighten up, thus leading to higher planetary irradiation and hence higher T_{eq} of their orbiting planets. However, alternative scenario that could explain HJ radius anomalies such as star–planet tidal interactions, which lead to internal heating of the planet, thus causing a radius inflation (e.g. see Fortney, Dawson & Komacek 2021, for a review).

Fig. 13 top compares giant planet equilibrium temperatures to their measured radii, where NGTS-21b presents a rather large radius when compared to HJs with similar $T_{eq} \sim 1300$ K, and also when compared to an inflation-free model (Thorngren & Fortney 2018), thus pointing to a possible inflated planet. The lower panel in the figure shows the lack of massive inflated HJs, which highlights the importance of confirming the inflated nature of NGTS-21b.

Table 4. Planetary properties for NGTS-21b.

Property	Value
P (d)	154 338 97 $\pm$ 0.0000016
T_C (BJD$_{TDB}$)	245 8228.77853 $\pm$ 0.000 67
T_{14} (h)	1.95 $\pm$ 0.03
a/R_s	5.89 $\pm$ 0.12
R_p/R_s	0.159 $\pm$ 0.003
b	0.63 $\pm$ 0.03
i(°)	83.85 $\pm$ 0.44
K (m s^{-1})	506 $\pm$ 37
e	0.0 (fixed)
ω (°)	90 (fixed)
Jitter (m s^{-1})	34^{+39}_{-21}
$M_p(M_J)$	2.36 $\pm$ 0.21
$R_p(R_J)$	1.33 $\pm$ 0.03
ρ_p (g cm^{-3})	1.25 $\pm$ 0.15
a (au)	0.0236 $\pm$ 0.0005
T^a_{eq} (K)	1357 $\pm$ 15

[a]Assumed zero Bond albedo.

Planetary structure models by Fortney, Marley & Barnes (2007, hereafter F07) predict NGTS-21b to have a radius $\sim$21 per cent smaller for an age of $\sim$3 Gyr, while Baraffe, Chabrier & Barman (2008, hereafter B08) inflation-free models, which take into account the metal mass fraction (Z) and its distribution within the planetary interior, predicts a radius of $\sim$21 per cent smaller at $Z = 0.02$ and no planet irradiation. We also compared B08 models that consider stellar irradiation, thus giving an $\sim$16 per cent smaller radius at 3 Gyr and Z = 0.02. Neither F07 nor B08 predict a radius consistent with observations, unless the planetary system is very young (100–500 Myr), where HJs radii are typically large, the models agree to our observed radius; yet we rejected the hypothesis that NGTS-21 is a young system (<1 Gyr) in Section 3.1.

To further confirm the inflated nature of the planet, we followed the method described in Costes et al. (2020), and based on Sestovic, Demory & Queloz (2018, hereafter S18), where an empirical model relating the expected radius inflation ΔR to planet radius, mass and incident fluxes derived from Bayesian statistical analysis on a sample of 286 transiting HJs. First, we estimated an incident flux (F) of $3.4 \pm 0.7 \times 10^6$ Wm^{-2} for NGTS-21b from Weiss et al. (2013), equation (9),

$$\frac{R_p}{R_\oplus} = 2.45 \left(\frac{M_p}{M_\oplus}\right)^{-0.039} \left(\frac{F}{\text{ergs s}^{-1}\text{ cm}^{-2}}\right)^{0.094} \quad (2)$$

which is valid for $M_p > 150\, M_\oplus$, and from S18 equation (11),

$$\Delta R = 0.52\,(\log_{10} F - 5.8)\,,\ 0.98 \leq \frac{M_p}{M_J} < 2.5 \quad (3)$$

we found a ΔR of 0.38 ± 0.05. The inflated radius is given by, $R_{inf} = C + \Delta R$, where C is the baseline radius from S18 equation (1), with best-fitting value of $1.06 \pm 0.03 R_J$ from S18 Table 1. Therefore, a R_{inf} of $1.44 \pm 0.06 R_J$ is expected for our estimated incidence flux on NGTS-21b , and is in statistical agreement to our measured radius from Table 4.

5 CONCLUSION

We report the discovery of NGTS-21b, a hot Jupiter with a mass, radius, and bulk density of $2.36 \pm 0.21 M_J$, $1.33 \pm 0.03 R_J$, and 1.25 ± 0.15 g cm^{-3}, respectively. The planet orbits a K3V star every 1.5 d, representing one of the shortest period gas giants orbiting such a low-mass star, and its large mass also makes it one of the most massive HJs orbiting such a star. We also find the planet to be inflated by around 21 per cent when comparing to inflation-free planetary structure models, and is significantly larger than other similar gas giants with effective temperatures in agreement with that of NGTS-21b. The close proximity of the planet to its host star means that a combination of stellar irradiation and tidal heating could explain the inflated nature of the planet's atmosphere.

When placing NGTS-21b in the metallicity versus planet bulk density plane for HJs, we identify a falling upper boundary in the metal-poor regime. The density of HJs decrease as a function of host star metallicity, which likely reflects the formation pathway for these planets. The large cores that are required to explain their high densities, drop in mass as a function of decreasing metallicity, since there exists less metals in the protoplanetary disc to quickly form larger cores through core accretion before the disc disperses. This decrease in core mass then returns a decrease in their bulk densities too. We fit two empirical models to this upper envelope in order to better characterize the effect. We also find weak evidence for the existence of a gap in this part of the parameter space, yet more observations and better statistics are required to confirm the gap's existence.

The host star NGTS-21 shows moderately low activity, as evidenced by the light curves low spot modulation amplitudes, and absence of flare activity. Moreover, its age of $10.02^{+3.29}_{-7.30}$ Gyr and rotation period 17.88 ± 0.08 d are in accordance with expected ages of 1.0−4.5 Gyr from gyrochronology models. A second rotation period was detected in the LS periodogram, thus indicating that NGTS-21 exhibits evidence for differential rotation. The planet's transit times were extracted and fitted by a linear ephemeris model, with residuals showing no transit time variations. In addition, light-curve eyeballing and BLS methods do not return any evidence of an additional companion in the system.

The discovery of NGTS-21b will add to the small yet increasing population of massive HJ planets around low-mass and metal-poor stars, thus helping place further constraints on current formation and evolution model for such planetary systems.

ACKNOWLEDGEMENTS

Based on data collected under the NGTS project at the ESO La Silla Paranal Observatory. The NGTS facility is operated by the consortium institutes with support from the UK Science and Technology Facilities Council (STFC) under projects ST/M001962/1, ST/S002642/1, and ST/W003163/1. This study is based on observations collected at the European Southern Observatory under ESO programme 105.20G9. DRA acknowledges support of ANID-PFCHA/Doctorado Nacional-21200343, Chile. JSJ greatfully acknowledges support by FONDECYT grant 1201371 and from the ANID BASAL projects ACE210002 and FB210003. JIV acknowledges support of CONICYT-PFCHA/Doctorado Nacional-21191829. Contributions at the University of Geneva by ML, FB and SU were carried out within the framework of the National Centre for Competence in Research 'PlanetS' supported by the Swiss National Science Foundation (SNSF). The contributions at the University of Warwick by PJW, SG, DB and RGW have been supported by STFC through consolidated grants ST/P000495/1 and ST/T000406/1. The contributions at the University of Leicester by MGW and MRB have been supported by STFC through consolidated grant ST/N000757/1.

CAW acknowledges support from the STFC grant ST/P000312/1. TL was also supported by STFC studentship 1226157. MNG acknowledges support from the European Space Agency (ESA) as an ESA Research Fellow. This project has received funding from the European Research Council (ERC) under the European Union's Horizon 2020 research and innovation programme (grant agreement No 681601). The research leading to these results has received funding from the European Research Council under the European Union's Seventh Framework Programme (FP/2007-2013)/ERC Grant Agreement n. 320964 (WDTracer). The contribution of ML has been carried out within the framework of the NCCR PlanetS supported by the Swiss National Science Foundation under grants 51NF40_182901 and 51NF40_205606. ML also acknowledges support of the Swiss National Science Foundation under grant number PCEFP2_194576.

DATA AVAILABILITY

The data underlying this article are made available in its online supplementary material.

REFERENCES

Adams F. C., Laughlin G., 2006, ApJ, 649, 1004
Agol E., Steffen J., Sari R., Clarkson W., 2005, MNRAS, 359, 567
Allard F., Homeier D., Freytag B., 2012, Phil. Trans. Roy. Soc. A: Math., Phys. Eng. Sci., 370, 2765
Almenara J. M. et al., 2018, A&A, 615, A90
Angus R. et al., 2019, AJ, 158, 173
Angus R., Morton T., Aigrain S., Foreman-Mackey D., Rajpaul V., 2018, MNRAS, 474, 2094
Baraffe I., Chabrier G., Barman T., 2008, A&A, 482, 315 (B08)
Barbary K., 2016, J. Open Source Software, 1, 58
Barbato D. et al., 2019, A&A, 621, A110
Barnes S. A., 2007, ApJ, 669, 1167
Barros S. et al., 2014, A&A, 561, L1
Batalha N. M. et al., 2011, ApJ, 729, 27
Bayliss D. et al., 2018, MNRAS, 475, 4467
Bayliss D. et al., 2022, X-Ray, Optical, and Infrared Detectors for Astronomy X, vol. 12191. SPIE. p. 441
Bonfils X. et al., 2013, A&A, 549, A109
Bouvier J., Matt S. P., Mohanty S., Scholz A., Stassun K. G., Zanni C., 2014, in Beuther H.., Klessen R. S., Dullemond C. P., Henning T., eds,Protostars and Planets VI, vol. 433. Univ. Arizona Press, Tucson, AZ, p. 94
Brasseur C. E., Phillip C., Fleming S. W., Mullally S. E., White R. L., 2019, Astrophysics Source Code Library, record ascl:1905.007
Briegal J. T. et al., 2022b, MNRAS, 513, 420
Briegal J., gds38 RoTo CI bot, 2022a, joshbriegal/roto: RoTo v0.1
Brown A. G. et al., 2021, A&A, 649, A1
Bryant E. M. et al., 2020, MNRAS, 499, 3139
Bryant E. M. et al., 2021, MNRAS, 504, L45
Buchhave L. A., Bitsch B., Johansen A., Latham D. W., Bizzarro M., Bieryla A., Kipping D. M., 2018, ApJ, 856, 37
Castelli F., Kurucz R. L., 2004, preprint (astro-ph/0405087)
Chazelas B. et al., 2012, Ground-based and Airborne Telescopes IV, vol. 8444. SPIE, p. 109
Christensen-Dalsgaard J., Aguirre V. S., 2018, preprint (arXiv:1803.03125)
Cochran W. D. et al., 2011, ApJS, 197, 7
Collier Cameron A. et al., 2006, MNRAS, 373, 799
Coppejans R. et al., 2013, Publ. Astron. Soc. Pac., 125, 976
Costes J. C. et al., 2020, MNRAS, 491, 2834
Cumming A., Butler R. P., Marcy G. W., Vogt S. S., Wright J. T., Fischer D. A., 2008, Publ. Astron. Soc. Pac., 120, 531

Demory B.-O., Seager S., 2011, ApJS, 197, 12
Dotter A., 2016, ApJS, 222, 8
Edelson R., Krolik J., 1988, ApJ, 333, 646
Epstein C. R., Pinsonneault M. H., 2013, ApJ, 780, 159
Espinoza N., Kossakowski D., Brahm R., 2019, MNRAS, 490, 2262
Feroz F., Hobson M., Bridges M., 2009, MNRAS, 398, 1601
Fischer D. A., Valenti J., 2005, ApJ, 622, 1102
Fortney J. J., Dawson R. I., Komacek T. D., 2021, J. Geophys. Res.: Planets, 126, e2020JE006629
Fortney J. J., Marley M. S., Barnes J. W., 2007, ApJ, 659, 1661 (F07)
Fulton B. J., Petigura E. A., Blunt S., Sinukoff E., 2018, Publ. Astron. Soc. Pac., 130, 044504
Gillen E. et al., 2020, MNRAS, 492, 1008
Gillon M. et al., 2017, Nature, 542, 456
Ginsburg A. et al., 2019, AJ, 157, 98
Gonzalez G., 1997, MNRAS, 285, 403
Hartman J. D. et al., 2016, AJ, 152, 182
Hauschildt P. H., Allard F., Baron E., 1999, ApJ, 512, 377
Henden A., Munari U., 2014, Contrib. Astron. Obs. Skalnate Pleso, 43, 518
Higson E., Handley W., Hobson M., Lasenby A., 2019, Statis. Comput., 29, 891
Holczer T. et al., 2016, ApJS, 225, 9
Hsu D. C., Ford E. B., Ragozzine D., Ashby K., 2019, AJ, 158, 109
Husser T.-O., Wende-von Berg S., Dreizler S., Homeier D., Reiners A., Barman T., Hauschildt P. H., 2013, A&A, 553, A6
Jenkins J. S. et al., 2017, MNRAS, 466, 443
Jenkins J., 2019, AAS/Division for Extreme Solar Systems Abstracts, 51, 103
Johnson J. A., Aller K. M., Howard A. W., Crepp J. R., 2010, Publ. Astron. Soc. Pac., 122, 905
Johnson J. A., Butler R. P., Marcy G. W., Fischer D. A., Vogt S. S., Wright J. T., Peek K. M., 2007, ApJ, 670, 833
Jones M. et al., 2016, A&A, 590, A38
Kawaler S. D., 1988, ApJ, 333, 236
Kipping D. M., 2013, MNRAS, 435, 2152
Kovács G., Zucker S., Mazeh T., 2002, A&A, 391, 369
Kreidberg L., 2015, Publ. Astron. Soc. Pac., 127, 1161
Kurucz R.-L., 1993, Kurucz CD-Rom, 13
Lithwick Y., Xie J., Wu Y., 2012, ApJ, 761, 122
Mamajek E. E., Hillenbrand L. A., 2008, ApJ, 687, 1264
Martins B. C. et al., 2020, ApJS, 250, 20
Mayor M. et al., 2003, The Messenger, 114, 20
Mayor M., Queloz D., 1995, Nature, 378, 355
McCormac J. et al., 2017, Publ. Astron. Soc. Pac., 129, 025002
McCormac J. et al., 2020, MNRAS, 493, 126
McQuillan A., Mazeh T., Aigrain S., 2014, ApJS, 211, 24
Meibom S., Mathieu R. D., Stassun K. G., 2009, ApJ, 695, 679
Miller N., Fortney J. J., 2011, ApJ, 736, L29
Mortier A., Santos N., Sozzetti A., Mayor M., Latham D., Bonfils X., Udry S., 2012, A&A, 543, A45
Morton T. D., 2015, Astrophysics Source Code Library. p. ascl–1503
Osborn A., Bayliss D., 2020, MNRAS, 491, 4481
Raynard L. et al., 2018, MNRAS, 481, 4960
Rebull L. et al., 2016, AJ, 152, 113
Reffert S., Bergmann C., Quirrenbach A., Trifonov T., Künstler A., 2015, A&A, 574, A116
Ricker G. R. et al., 2015, J. Astron. Telesc. Instrum. Syst., 1, 014003
Santos N., Israelian G., Mayor M., 2001, A&A, 373, 1019
Sestovic M., Demory B.-O., Queloz D., 2018, A&A, 616, A76 (S18)
Skrutskie M. F. et al., 2006, AJ, 131, 1163
Sneden C., 1973, ApJ, 184, 839
Soto M., Jenkins J. S., 2018, A&A, 615, A76
Sousa S., Santos N. C., Israelian G., Mayor M., Monteiro M., 2007, A&A, 469, 783
Southworth J., 2011, MNRAS, 417, 2166
Speagle J. S., 2020, MNRAS, 493, 3132
Stassun K. G. et al., 2018, AJ, 156, 102
Steffen J. H. et al., 2012a, Proc. Natl. Acad. Sci., 109, 7982
Steffen J. H. et al., 2012b, MNRAS, 421, 2342
Tamuz O., Mazeh T., Zucker S., 2005, MNRAS, 356, 1466
Thorngren D. P., Fortney J. J., 2018, AJ, 155, 214
Tilbrook R. H. et al., 2021, MNRAS, 504, 6018
VanderPlas J. T., 2018, ApJS, 236, 16
VanderPlas J. T., Ivezic Ž., 2015, ApJ, 812, 18
Vines J. I. et al., 2019, MNRAS, 489, 4125
Vines J. I., Jenkins J. S., 2022, MNRAS, 513, 2719
Weiss L. M. et al., 2013, ApJ, 768, 14
West R. G. et al., 2019, MNRAS, 486, 5094
Wheatley P. J. et al., 2018, MNRAS, 475, 4476
Wright E. L. et al., 2010, AJ, 140, 1868
Wright J., Marcy G., Howard A., Johnson J. A., Morton T., Fischer D., 2012, ApJ, 753, 160
Yee S. W. et al., 2019, ApJ, 888, L5

SUPPORTING INFORMATION

Supplementary data are available at *MNRAS* online.

Table 1. NGTS, TESS, and SAAO photometry for NGTS-21.
Figure 10. NGTS-21b computed TTV.

Please note: Oxford University Press is not responsible for the content or functionality of any supporting materials supplied by the authors. Any queries (other than missing material) should be directed to the corresponding author for the article.

[1]*Departamento de Astronomía, Universidad de Chile, Casilla 36-D, 7591245, Santiago, Chile*
[2]*Centro de Astrofísica y Tecnologías Afines (CATA), Casilla 36-D, 7591245, Santiago, Chile*
[3]*Núcleo de Astronomía, Facultad de Ingeniería y Ciencias, Universidad Diego Portales, Av. Ejército 441 Santiago, Chile*
[4]*European Southern Observatory (ESO), Karl-Schwarzschild-Straße 2, D-85748 Garching bei München, Germany*
[5]*Department of Physics, University of Warwick, Gibbet Hill Road, Coventry CV4 7AL, UK*
[6]*Centre for Exoplanets and Habitability, University of Warwick, Gibbet Hill Road, Coventry CV4 7AL, UK*
[7]*School of Physics and Astronomy, University of Leicester, Leicester LE1 7RH, UK*
[8]*Departement d'Astronomie, Université de Genève, 51 chemin Pegasi, CH-1290 Sauverny, Switzerland*
[9]*South African Astronomical Observatory, PO Box 9, Observatory 7935 Cape Town, South Africa*
[10]*Department of Astronomy, University of Cape Town, Rondebosch 7700 Cape Town, South Africa*
[11]*Mullard Space Science Laboratory, University College London, Holmbury St Mary, Dorking, Surrey RH5 6NT, UK*
[12]*Department of Extrasolar Planets and Atmospheres, Institute of Planetary Research, German Aerospace Center (DLR), Rutherfordstraße 2, D-12489 Berlin, Germany*
[13]*Astronomy Unit, Queen Mary University of London, Mile End Road, London E1 4NS, UK*
[14]*Astrophysics Group, Cavendish Laboratory, J.J. Thomson Avenue, Cambridge CB3 0HE, UK*
[15]*European Space Agency (ESA), European Space Research and Technology Centre (ESTEC), Keplerlaan 1, NL-2201 AZ Noordwijk, the Netherlands*
[16]*Instituto de Astronomía, Universidad Católica del Norte, Casa Central, Angamos 0610 Antofagasta, Chile*
[17]*Aix Marseille Univ, CNRS, CNES, LAM, Marseille, 13388, France*
[18]*Astrophysics Research Centre, School of Mathematics and Physics, Queen's University Belfast, BT7 1NN Belfast, UK*

This paper has been typeset from a TEX/LATEX file prepared by the author.